Non-invasive and low-artifact *in vivo* brain imaging by using a scanning acoustic-photoacoustic dual mode microscopy

Wentian Chen(陈文天), Chao Tao(陶超), Zizhong Hu(胡仔仲), Songtao Yuan(袁松涛),Qinghuai Liu(刘庆淮), and Xiaojun Liu(刘晓峻)

Citation: Chin. Phys. B, 2022, 31 (**4**): 044304. DOI: 10.1088/1674-1056/ac4a6f
Journal homepage: http://cpb.iphy.ac.cn; http://iopscience.iop.org/cpb

What follows is a list of articles you may be interested in

Deep learning for image reconstruction in thermoacoustic tomography

Qiwen Xu(徐启文), Zhu Zheng(郑铸), and Huabei Jiang(蒋华北)
Chin. Phys. B, 2022, 31 (**2**): 024302. DOI: 10.1088/1674-1056/ac0dab

Influence of mode conversions in the skull on transcranial focused ultrasound and temperature fields utilizing the wave field separation method: A numerical study

Xiang-Da Wang(王祥达), Wei-Jun Lin(林伟军), Chang Su(苏畅), Xiu-Ming Wang(王秀明)
Chin. Phys. B, 2018, 27 (**2**): 024302. DOI: 10.1088/1674-1056/27/2/024302

Noninvasive treatment efficacy monitoring and dose control for high-intensity focused ultrasound therapy using relative electrical impedance variation

Huidan Su(宿慧丹), Gepu Guo(郭各朴), Qingyu Ma(马青玉), Juan Tu(屠娟), Dong Zhang(章东)
Chin. Phys. B, 2017, 26 (**5**): 054302. DOI: 10.1088/1674-1056/26/5/054302

Impact of cavitation on lesion formation induced by high intensity focused ultrasound

Pengfei Fan(范鹏飞), Jie Yu(于洁), Xin Yang(杨鑫), Juan Tu(屠娟), Xiasheng Guo(郭霞生), Pintong Huang(黄品同), Dong Zhang(章东)
Chin. Phys. B, 2017, 26 (**5**): 054301. DOI: 10.1088/1674-1056/26/5/054301

A new brain stimulation method: Noninvasive transcranial magneto-acoustical stimulation

Yi Yuan(袁 毅), Yu-Dong Chen(陈玉东), Xiao-Li Li(李小俚)
Chin. Phys. B, 2016, 25 (**8**): 084301. DOI: 10.1088/1674-1056/25/8/084301

Non-invasive and low-artifact *in vivo* brain imaging by using a scanning acoustic-photoacoustic dual mode microscopy

Wentian Chen(陈文天)[1], Chao Tao(陶超)[1,†], Zizhong Hu(胡仔仲)[2], Songtao Yuan(袁松涛)[2,‡], Qinghuai Liu(刘庆淮)[2], and Xiaojun Liu(刘晓峻)[1,§]

[1] *Ministry-of-Education Key Laboratory of Modern Acoustics, Department of Physics, Collaborative Innovation Center of Advanced Microstructures, Nanjing University, Nanjing* 210093, *China*
[2] *Department of Ophthalmology, The First Affiliated Hospital of Nanjing Medial University, Nanjing* 210029, *China*

(Received 20 August 2021; revised manuscript received 25 November 2021; accepted manuscript online 12 January 2022)

Photoacoustic imaging is a potential candidate for *in vivo* brain imaging, whereas, its imaging performance could be degraded by inhomogeneous multi-layered media, consisted of scalp and skull. In this work, we propose a low-artifact photoacoustic microscopy (LAPAM) scheme, which combines conventional acoustic-resolution photoacoustic microscopy with scanning acoustic microscopy to suppress the reflection artifacts induced by multi-layers. Based on similar propagation characteristics of photoacoustic signals and ultrasonic echoes, the ultrasonic echoes can be employed as the filters to suppress the reflection artifacts to obtain low-artifact photoacoustic images. Phantom experiment is used to validate the effectiveness of this method. Furthermore, LAPAM is applied for *in-vivo* imaging mouse brain without removing the scalp and the skull. Experimental results show that the proposed method successfully achieves the low-artifact brain image, which demonstrates the practical applicability of LAPAM. This work might improve the photoacoustic imaging quality in many biomedical applications which involve tissues with complex acoustic properties, such as brain imaging through scalp and skull.

Keywords: photoacoustic microscopy, scanning acoustic microscopy, noninvasive, low-artifact, brain imaging

PACS: 43.35.Ud, 43.35.Sx, 78.20.Pa, 81.70.Cv **DOI:** 10.1088/1674-1056/ac4a6f

1. Introduction

Photoacoustic microscopy (PAM) is a potential brain imaging modality, benefitting from the advantages of rich functional information in biological tissue.[1–10] PAM is based on the photoacoustic (PA) effect. Short laser pulse illuminates the biological tissues. Laser energy absorption of optical absorbers causes thermal expansion and emission of the ultrasound waves, i.e., PA waves. A spherically focused ultrasonic (US) transducer is implemented to detect the PA waves. One-dimensional (1D) image along the transducer axis can be formed according to the time-of-flight and intensity of the signals. A three-dimensional (3D) image can be obtained by point-by-point scanning the object along a two-dimensional plane. When the imaging depth exceeds the optical mean free path ($\sim$ 1 mm), the size of the acoustical focus is smaller than that of the optical focus. In this situation, the lateral resolution of PAM is determined by the acoustical focus. This imaging modality is known as an acoustic-resolution PAM (AR-PAM). AR-PAM breaks the limitation of optical diffusion and provides acoustic-resolution (a few tens to hundreds of micrometers) in deep tissue, which promises it a very wide range of applications, such as cancer detection,[11,12] *in vivo* brain imaging of small animals,[13–17] flow velocity monitoring,[18–20] and so on.[21–32]

However, AR-PAM still faces the challenges of imaging through inhomogeneous multilayered media. When imaging optical absorbers below several acoustically inhomogeneous layers, the acoustic impedance mismatch between these layers could cause multiple reflections of PA signals. The reflections form artifacts in the images. These artifacts are mixed with real images of the objects and make real information hard to be distinguished. Therefore, the existence of reflections induced by multilayered impedance mismatch is still an obstacle that significantly restricts the imaging performance of AR-PAM, especially in the field of noninvasive *in vivo* brain imaging of small animals since high acoustic impedance of skull, scalp, and so on.

Some methods have been reported to reduce the reflection artifacts induced by acoustic reflection layers.[33–37] By mimicking PA wave fields using an US wave, the artifacts of the optical absorbers above the one-layer-reflector are reduced in a PA tomography.[33,34] Convolutional neural network has also been trained to locate both sources and reflection artifacts, and suppress the artifacts in the PA channel data.[35] Multiple-wavelengths illumination is also utilized to identify and remove the reflection artifacts based on the correlation between the reflections and their corresponding original images.[36] Also, our previous work presented an US-guided

†Corresponding author. E-mail: taochao@nju.edu.cn
‡Corresponding author. E-mail: yuansongtao@vip.sina.com
§Corresponding author. E-mail: liuxiaojun@nju.edu.cn

PAM to reduce the reflection artifacts induced by a bone-like layer.[37] However, the problem of artifacts induced by multilayered media above the optical absorbers in PAM has not been well addressed. Multilayered scattering is still a significant factor that restricts the performance of brain imaging.

In this work, we propose a method called low-artifact PAM (LAPAM), which combines conventional AR-PAM with scanning acoustic microscopy (SAM) to suppress the reflection artifacts induced by multi-layers. First, we derive the general transfer function of PA waves and US echoes with the existence of multi-layers. The derived transfer function reveals the similar propagation scheme of PA waves and US echoes. Then, according to this finding, we propose a LAPAM theory based on the scanning acoustic-photoacoustic (SA-PA) dual mode microscopy. In this theory, the US signals can be treated as the transfer functions of the reflection scheme, and the PA signals can be finally deconvolved by the transfer functions to get the low-artifact results. In other words, the US signals can be implemented to guide the PA imaging and suppress the artifacts in the image. A phantom experiment is used to demonstrate the imaging process and validation of LAPAM. Finally, *in vivo* brain imaging experiment is employed to examine the practical applicability of LAPAM.

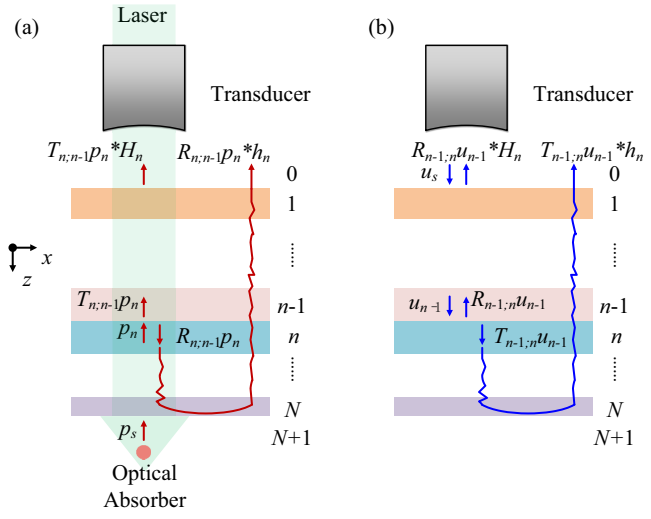

Fig. 1. Scheme of the proposed method considering N different reflection layers. Here, we mark the area below layer N as layer $N+1$, and area above layer 1 as layer 0. (a) The process of the PA excitation, propagation, and detection. Supposing that the strongest acoustic impedance mismatch occurs between the layers $n-1$ and n, we neglect the reflections induced by other interfaces. p_s: the PA signal emitted from the optical absorber; p_n: the incident wave from layer n to $n-1$; h_n: the impulse response of multilayers when multilayered reflections act on the reflected wave of p_n. H_n: the impulse response that performs on the transmitted wave of p_n. (b) The model of the US emission, propagation and detection. u_s: the PA signal emitted from the transducer; u_{n-1}: the incident wave from layer $n-1$ to n. From the simplified scheme in (a) and (b), we can see that the PA signal and the US echo share similar propagation characteristics.

2. Methods

Let us compare the acoustic wave propagation characteristics in multilayered media with N different layers, as shown in Fig. 1. Assuming the acoustic impedance of layer n ($n=0,1,2,\ldots,N+1$; here, we mark the area below layer N as layer $N+1$, and area above layer 1 as layer 0) is r_n, when the acoustic wave propagates from layer n to layer n', the reflection coefficient $R_{n;n'}$ and transmission coefficient $T_{n;n'}$ can be given as $R_{n;n'}=(r_{n'}-r_n)/(r_{n'}+r_n)$ and $T_{n;n'}=2r_{n'}/(r_{n'}+r_n)$ with $|n-n'|=1$ and $n,n'=1,2,\ldots,N$, where $r_{n'}$ and r_n represent the acoustic impedance of layers n' and n, respectively. The transducer emits US waves above the multilayered media and detects US echoes on the same side. The PA excitation is implemented on the optical absorbers below the acoustic reflection layers to generate PA signals. When the PA signals pass through the multilayered media, multi-reflections will occur and these signals mixed with the reflected waves are received by the upper transducer. Actually, the interface with strongest acoustic impedance mismatch plays the most important role in the appearance of reflections and artifacts. Based on this and without loss of generality, we give two fundamental assumptions before considering the PA/US propagations through multilayers:

Assumption (1): The reflections above the layer $n-1$ is weak ($|R_{i;i-1}|$ or $|R_{i-1;i}| \ll 1$ when $i=1,2,\ldots,n-1$), like the layers with weak reflections above the interface between the scalp and the skull.

Assumption (2): We suppose that the strongest acoustic impedance mismatch occurs between the layers $n-1$ and n. And only the strongest reflection and artifacts related to their interface are considered here.

Based on the two assumptions above, we first consider the PA signal passing through the inhomogeneous layers, as shown in Fig. 1(a). $p_s(t)$ is the PA signal emitted from an optical absorber below the inhomogeneous layer. And $p(t)$ is the signal detected by a US transducer above the inhomogeneous layer. Let $p_n(t)$ be the incident wave from layer n to $n-1$. Since the PA wave $p_s(t)$ has passed through all interface below layer n, it has the relationship $p_n(t)=a_n p_s(t)$ with $a_n=\Pi_{i=n}^{N}T_{i+1;i}$. Finally, its reflected wave passes through a complex path and also arrives at the US transducer. Write the impulse path of this complex propagation path as $h_n(t)$, a series of reflected wave components originating from the reflected wave of $p_n(t)$ (i.e., $R_{n;n-1}p_n(t)$) can be treated as the convolution between $R_{n;n-1}p_n(t)$ and the response of a linear system, that is, $R_{n;n-1}p_n(t)*h_n(t)$. Here "$*$" refers to the convolution operation. Also, the transmitted wave of $p_n(t)$ (i.e., $T_{n;n-1}p_n(t)$) passes through the path $H_n(t)$. The detected PA signal $p(t)$ can be written as $p(t)=T_{n;n-1}p_n(t)*H_n(t)+R_{n;n-1}p_n(t)*h_n(t)$. According to the two assumptions above, the high-order reflections in $H_n(t)$ can be ignored. Therefore, we have

$$p(t)\approx a_0 p_s(t)+R_{n;n-1}a_n p_s(t)*h_n(t) \tag{1}$$

with $a_n = \Pi_{i=n}^{N} T_{i+1;i}$. Further, Eq. (1) can be rewritten as

$$p(t) \approx a_n p_s(t) * \left[a'_n \delta(t) + R_{n;n-1} h_n(t)\right] \tag{2}$$

with $a'_n = \Pi^{n-1}{}_{i=0} T_{i+1;i}$.

Second, let us investigate the US wave reflected from the inhomogeneous layer, as shown in Fig. 1(b). We also consider the US interaction on the interface between the layers $n-1$ and n, as shown in Fig. 1(b). Write the incident wave from layer $n-1$ to n as $u_{n-1}(t)$, it has $u_{n-1}(t) = b_{n-2} \cdot u_s(t)$ with $b_{n-2} = \Pi^{n-2}{}_{i=0} T_{i;i+1}$. Similarly, the reflected wave and the transmitted wave will eventually arrive at the transducer by passing the complex path $h_n(t)$ and $H_n(t)$, respectively. The echo signal can be written as $u(t) = R_{n-1;n} u_{n-1}(t) * H_n(t) + T_{n-1;n} u_{n-1}(t) * h_n(t)$. Ignoring the reflections above layer $n-1$ based on assumption (1), we have

$$u(t) \approx a'_{n-1} R_{n-1;n} b_{n-2} u_s(t) + b_{n-1} u_s(t) * h_n(t) \tag{3}$$

with $b_{n-2} = \Pi^{n-2}{}_{i=0} T_{i;i+1}$, $a'_{n-1} = \Pi^{n-2}{}_{i=0} T_{i+1;i}$. Equation (3) can be rewritten as

$$u(t) \approx b_{n-2} u_s(t) * [R_{n-1;n} a'_{n-1} \delta(t) + T_{n-1;n} h_n(t)]. \tag{4}$$

Here, we further rewrite Eq. (4) as

$$u(t) \propto b_{n-2} u_s(t) * [C a'_n \delta(t) + R_{n;n-1} h_n(t)] \tag{5}$$

with $C = R_{n;n-1} R_{n-1;n} / T_{n;n-1} T_{n-1;n}$. Here "$\propto$" means "proportional to".

Comparing Eqs. (2) and (5), it can be noticed that the US pulse $u_{n-1}(t)$ passes through the same path as PA impulse $p_n(t)$ in the proposed model. Therefore, the US echo could be implemented to estimate the transfer function of PA signals. Using the estimated transfer function, the reflected waves can be removed, and the original PA signal $p_s(t)$ could be recovered from the detected signal $p(t)$. This is the basic idea of LAPAM. LAPAM combines conventional AR-PAM and SAM. And its detailed image strategy can be implemented as the following steps:

Step 1 Estimate the impulse response of the PA signal reflections from the US echo $u(t)$. Rewriting Eq. (2), we have $p(t) = p_s(t) * h_{pa}(t)$ with $h_{pa}(t) \propto a'_n \delta(t) + R_{n;n-1} h_n(t)$. Similarly, rewriting Eq. (5), we have $u(t) = u_s(t) * h_{us}(t)$ with $h_{us}(t) \propto C a'_n \delta(t) + R_{n;n-1} h_n(t)$. It can be found that their coefficients of each corresponding terms in the transfer function $h_{us}(t)$ and $h_{pa}(t)$ are the same, except of the first term. Modifying the strongest peak in the detected US signal $u(t)$ by multiplying a correction factor $(1/C)$, we can obtain a reference signal $U(t)$ as

$$U(t) = \begin{cases} \frac{1}{C} u(t), & -\frac{R_a}{c} \le t - \arg\max_t |\text{Hilbert}[u(t)]| \le \frac{R_a}{c}, \\ u(t), & t - \arg\max_t |\text{Hilbert}[u(t)]| > \frac{R_a}{c}, \end{cases} \tag{6}$$

where Hilbert[•] refers to the Hilbert transform operator. The maximum of the modulus of the Hilbert transform is used here to get the peak of the signal envelope. And R_a is the axial resolution of the US transducer and c is the speed of sound in tissue. Thus, $U(t) \propto u_s(t) * h_{pa}(t)$.

While in the spectral domain, the relationship between $U(t)$ and $u_s(t)$ can be rewritten as $F(U) = F(u_s) F(h_{pa})$, where $F[\bullet]$ represents the Fourier transform operator. Then, the impulse response of the multilayers h_{pa} in the spectral domain can be obtained by

$$F(h_{pa}) = \frac{F(U) W(\omega)}{F(u_s)}, \tag{7}$$

where $W(\omega)$ is a windowing function to prevent the amplification of frequencies outside the transducer response. Such windowing function is the frequency spectrum of transducer impulse response, which has a central frequency of ~ 15 MHz and a relative bandwidth of 60% at -6 dB.

Step 2 Apply the deconvolution between $p(t)$ and h_{pa} to suppress the components of the multiple reflections in the PA signal as

$$P(t) = F^{-1}\left[\frac{F(p) W(\omega)}{F(h_{pa})}\right], \tag{8}$$

where $F^{-1}[\bullet]$ represents the inverse Fourier transform, and $P(t) \propto p_s(t)$ is the low-artifact result.

Step 3 An A-line image at this scanning position can be obtained by $A(x, y; z) = P(z)$ with $z = ct$, where c is the speed of sound in tissue.

Step 4 For each position in the scanning plane (x, y), the above steps are repeated to achieve three-dimensional PA images $A(x, y, z)$. The LAPAM image $A(x, y, z)$ describes the distribution of the optical absorbers.

3. Experimental systems

Figure 2(a) shows the schematic diagram of the experimental setup. Laser pulse (wavelength: 532 nm, repetition rate: 10 kHz, pulse duration: ~ 8 ns) was emitted from a neodymium-doped yttrium aluminum garnet (Nd: YAG) laser (Spectra-Physics, EXPL-532-2Y). The energy of each laser pulse is ~ 100 μJ and the laser beam was coupled into an optical fiber bundle composed of 19 fibers via a convex lens. Exit ends of these fibers were mounted by a customized 3D printed fiber-transducer holder, as shown in Figs. 2(b) and 2(c). A focused US transducer was fixed in the center of the fiber-transducer holder. And exit ends of the optic fibers were mounted around the transducer evenly along a circle. The angle between each fiber and the horizontal plane is 50°. So that, exit beams were converged at the acoustic focus to ensure the optimal sensitivity of PA signal generation and detection. Since the diameter of the light spot illuminated on the sample surface is about ~ 4 mm, the optical fluence is about ~ 0.80 mJ/cm^2, less than the American National Standards Institute (ANSI) safety limit for 400–700 nm (20 mJ/cm^2).

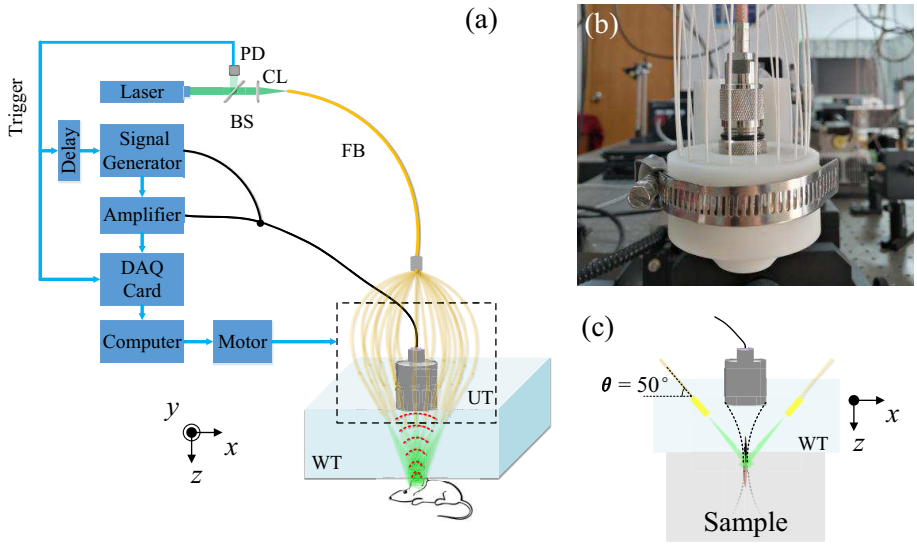

Fig. 2. The experimental setup. (a) The schematic diagram of the dual-mode microscope system. DAQ card, data acquisition card; BS, beam splitter; PD, photodiode; CL, convex lens; WT, water tank; UT, ultrasonic transducer; FB, fiber bundle. The part in the dotted frame is the fiber-transducer holder. (b) The photograph of the fiber-transducer holder. (c) The arrangement of optic fibers and US transducer in the fiber-transducer holder. The angle between each fiber and the horizontal plane θ is 50°. The exit beams are converged at the acoustic focus to ensure the optimal sensitivity of PA signal generation and detection.

The same US transducer was also used to generate US pulse and detect US echoes. In our experiment, the spherical transducer (Olympus NDT, V319-SU-F) with a central frequency of 15 MHz, a focal length of 19 mm, and a relative bandwidth of 60% at −6 dB was used to emit US pulses and detect PA signals/US echoes. When detecting PA/US signals, the US transducer and the ends of the fiber were immersed into the water tank to ensure good acoustic coupling. The bottom of the water tank was sealed with a polydimethylsiloxane (PDMS) layer for waterproofing and good light transmission. An electrical impulse produced by the pulse generator (Goworld, CTS-8077PR) was applied on the transducer to emit US pulse. The detected PA/US signals were amplified by a low-noise amplifier with a gain of ∼ 46 dB and digitized by a data acquisition card (National Instruments, NI-5761) at a sampling frequency of 250 MHz. A photodiode (Thorlabs, PDA10AEC) was used to monitor the intensity of the laser pulse. Its output was also used as a time reference to trigger the data acquisition card and control the pulse generator. A two-dimensional motorized translational stage (Zolix Instruments, KSA050-11-X, PSA050-11-X) was driven by the motion controller (Zolix Instruments, MC600) to perform the x–y plane scanning. Figure 3 describes the time sequence of the laser emission, PA signal detection, US emission and US echo detection. Each period of PA/US emission and detection was triggered by the laser emission. 12 μs after laser emission, PA signal was recorded for a duration of 4 μs. Then, 20 μs after laser emission, US emission was emitted. US echo was recorded 24 μs after US emission (48 μs after laser emission). The duration of the recorded US echo is 8 μs. Repeating the above process, the system achieved three-dimensional PA and US image, simultaneously.

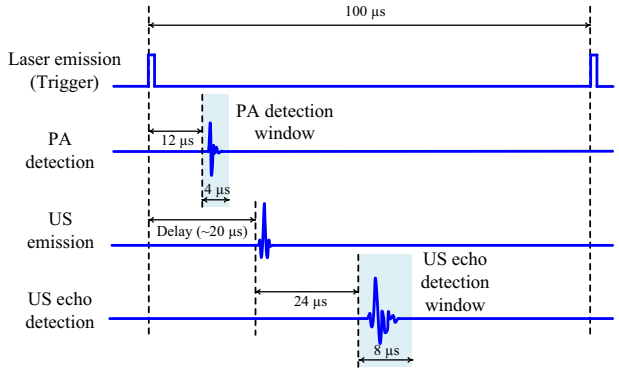

Fig. 3. Time sequence of the laser emission (trigger), PA detection, US emission and US echo detection. Each period of PA/US emission and detection starts from the laser emission.

4. Phantom experiment

The performance of the SA-PA dual mode microscopy was firstly examined by imaging five tungsten wires with a diameter of ∼ 100 μm. Figures 4(a) and 4(b) give the maximum amplitude projection (MAP) images of samples. Both AR-PAM image and SAM image can present the five tungsten wires clearly. Figure 4(c) gives the 1D normalized cross-sectional profiles of a tungsten wire, along the white dashed lines on (a) and (b). Red empty dots and black empty squares in Fig. 4(c) correspond to the PA image and US image, respectively. And their Gaussian fittings are given by the red solid line and black dashed line. The full widths at half maximum (FWHMs) of the tungsten wire images are about 288 ± 16 μm and 266 ± 13 μm for PAM and SAM, respectively. As the matter of fact, the image of an object is the result of convolution between the real shape of the object and the point spread function of the imaging system. The lateral resolution of the system can be estimated by extracting the real size of the object

from the FWHM.[38] Since the tungsten wire is not perpendicular to the x-axis, the actual size of the object in the 1D profile marked by the white dashed line should be equal to (real diameter/cos α), where α is the angle between the normal direction of the tungsten wire and the x-axis (α is an acute angle). Here, since $\cos\alpha = 0.97$ and the real diameter of the tungsten wire is ~ 100 μm, the actual size $= 100$ μm/0.97 $= 103$ μm. As a matter of fact, the lateral resolution of the system can be estimated by extracting the actual size of the object from the FWHM. Based on this, the lateral resolutions of PAM and SAM are estimated to be about 185 μm and 163 μm, which are closed to their theoretical values 183 μm and 150 μm.[39] From the result we can see that this test can successfully justify the effectiveness of the AR-PAM and SAM imaging modes.

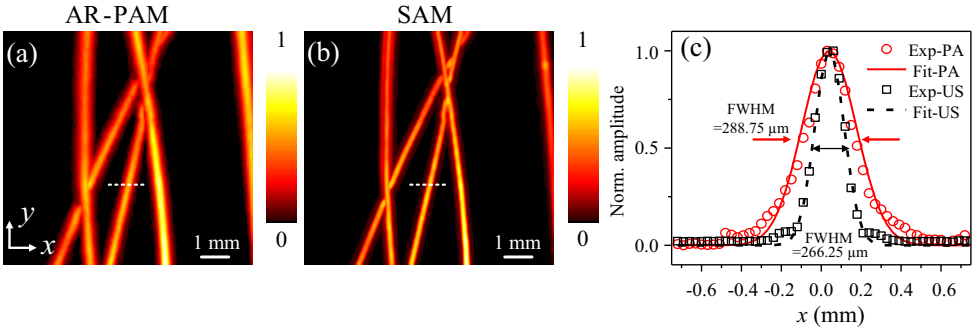

Fig. 4. The test of the dual-mode microscope by imaging tungsten wires. (a) The MAP image of the conventional AR-PAM. (b) The MAP of the SAM image. (c) The normalized 1D cross-sectional profiles of a tungsten wire, as indicated by the white dashed lines in (a) and (b). Red empty circle dots and black empty square dots indicate the 1D PA profile and US profile. Their Gaussian fittings are given by red solid line and black dashed line, respectively.

A phantom experiment was used to examine the ability of our proposed method for removing reflection artifacts induced by a multilayered cover. The phantom is made of six randomly arranged tungsten wires, which act as optical absorbers, something like the brain vessels below the scalp and the skull. A multilayered cover is fixed above the phantom. The cover consists of three reflection layers, which from top to bottom are PDMS layer, acrylic layer, and PDMS layer, respectively. Here, the top PDMS film layer has a thickness of ~ 0.5 mm, with acoustic impedance of about 1.08×10^6 kg/(m^2·s).[40] The middle layer is made of acrylic with a thickness of about 0.5 mm that is closed to the thickness of the skull of small animals. The acoustic impedance of the middle film is 3.24×10^6 kg/(m^2·s),[37] which is closed to that of the skull of small animals, but much higher than that of the surrounding water. The bottom layer is also made of PDMS and has a thickness of about 0.2 mm. In short, the cover has much higher acoustic impedance than the surrounding water, and its three layers have quite different acoustic impedances. Therefore, the cover induces complex and strong acoustic reflections, as well as the scalp, and the skull.

Figure 5 gives the typical waveforms obtained by conventional SAM, conventional AR-PAM, and LAPAM. Synthetic aperture focusing technique (SAFT) is used here to improve the image resolution and signal-to-noise ratio in out-of-focus regions, and consequently broadens the depth-of-field of the image. The black line in Fig. 5(a) shows a US echo waveform $u(t)$ obtained by SAM. The detected US echo has many reflected waves due to the impedance mismatch. The four highest peaks correspond to four interfaces between the three cover

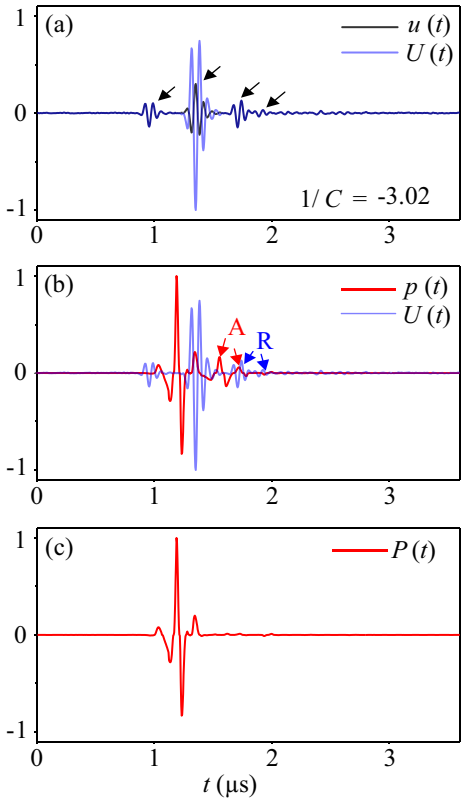

Fig. 5. The process of removing the reflected artifacts caused by three different reflecting layers in a typical A-line. (a) Comparison of typical waveform of the detected US echo $u(t)$ (black curves) and reference signal $U(t)$ (blue curves). The four peaks in $u(t)$ correspond to four interfaces of the layers. Here, we multiply the second peak of $u(t)$ with correction factor$1/C = -3.02$ to get $U(t)$. (b) Typical waveform of the PA signal $p(t)$ detected at the same position (red curves) and the reference signal $U(t)$, where the artifacts reflected by interface between layer 2 and layer 3, and interface between layer 3 and layer 4 are pointed out by red arrows. The corresponding reflection waves in $U(t)$ are marked by blue arrows. A: artifacts. R: reflections. (c) Typical low-artifact PA waveform $P(t)$ obtained by the proposed method.

layers and the surrounding water, as pointed out by black arrows. Then, considering that the second peak in US echo has the strongest amplitude among the reflection peaks, the reference signal $U(t)$ [blue line in Fig. 5(a)] can be derived from the simplified detected US echo $u(t)$ by modifying the second peak of $u(t)$ by correction factor $1/C = -3.02$ as $U(t) \propto u_s(t) * [(1/C)Ca_2'\delta(t) + R_{2;1}h_2(t)] = u_s(t) * [a_2'\delta(t) + R_{2;1}h_2(t)]$, according to the acoustic impedance of acrylic film and PDMS. The red line in Fig. 5(b) gives the PA signals $p(t)$ detected at the same position as the US echo $u(t)$. Besides the first peak, which is directly transmitted from the tungsten wires to the transducer, the left two peaks (pointed out by red arrows) come from reflections in the multilayered cover. For comparison, the waveform of $U(t)$ is plotted in Fig. 5(b) again and the corresponding reflection waves in $U(t)$ are marked by blue arrows. The similarity between $p(t)$ and $U(t)$ can be easily observed. Therefore, $U(t)$ can be utilized to estimate the transfer function in the spectral domain $F(h_{pa}) = F^{-1}[F(U)W(\omega)/F(u_s)]$ to suppress multiple reflections in PA waves. Figure 5(c) gives the signal $P(t) = F^{-1}[F(p)W(\omega)/F(h_{pa})]$ processed by our proposed method, where the reflected signals have been effectively suppressed.

Figure 6 gives the 3D rendering display of the phantom obtained by two-dimensional scanning along the x–y plane. The scanning range is 12 mm × 12 mm and the scanning step is 30 μm. The SAM image given in Fig. 6(a) indicates the interface profiles of the multilayers. The conventional AR-PAM image is given in Fig. 6(b). A mass of reflection

artifacts seriously degrade the quality of the image, and prevent the real information from being distinguished. The corresponding LA-PAM image obtained by the proposed method is shown in Fig. 6(c). We can see that the reflection artifacts have been effectively removed, while the real image of the optical absorbers in the phantom is kept.

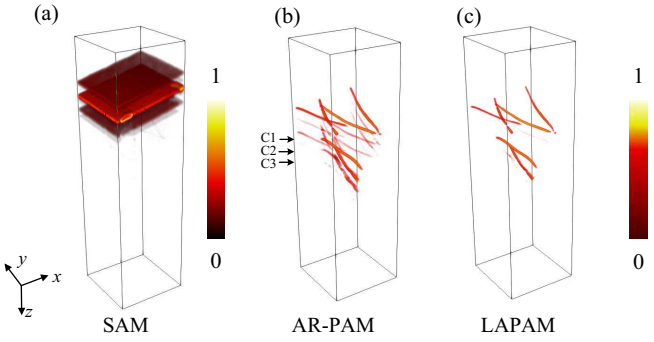

Fig. 6. The 3D rendering display of the phantom. (a) SAM image. (b) Conventional PAM. (c) LAPAM image. C1, C2, and C3 point out the positions of three slices in Fig. 7.

In order to show the advantage of LAPAM more clearly, we compare x–y cross sectional slices at three different layers achieved by different methods in Fig. 7. The top row [(a), (b)], the middle row [(c), (d)] and the bottom row [(e), (f)] correspond to the three different layers C1, C2, C3 indicated in Fig. 6. The distance between each layer is 0.6 mm. The three images at the left column [(a), (c), and (e)] are obtained by conventional AR-PAM, where many reflected artifacts are mixed with real images. Benefitting from our method, the quality of three images on the right column [(b), (d) and (f)] is strongly improved. The artifacts are suppressed and the real images are left. To conclude, the proposed method significantly suppresses the reflection artifacts and improves the image quality under the multilayered strong reflectors.

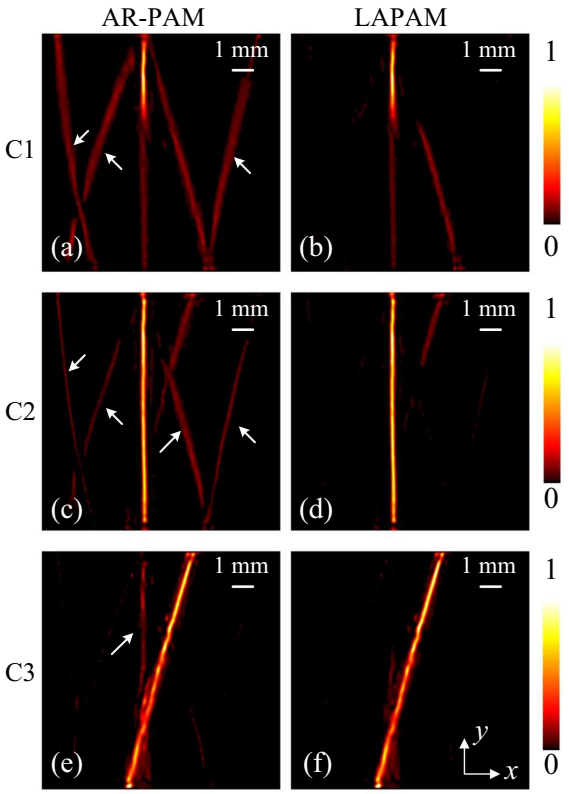

Fig. 7. Comparisons of the image obtained by conventional ARPAM and LAPAM at three different depths. The top [(a) and (b)], middle [(c) and (d)], and low [(e) and (f)] rows correspond to the layers of C1, C2, and C3 indicated in Fig. 6. The left column [(a), (c) and (e)] illustrates the conventional AR-PAM images with many reflection artifacts, which are indicated by white arrows. The right column [(b), (d) and (f)] gives the images obtained by the proposed method, where the artifacts are removed.

5. *In vivo* brain imaging experiments

We applied the proposed scheme to image mouse brain *in vivo*. Male nude mouse (around six weeks old and weighting ∼ 20 g) was selected as the animal model for *in vivo* imaging experiments. The mouse was initially anesthetized by using the isoflurane gas with a concentration of 3% in an induction box. After that, the mouse was moved onto the animal holder and maintained general anesthesia by breathing isoflurane gas through an anesthetic mask and an animal anesthesia machine. The isoflurane gas had a concentration of 3% during the experiments. Before imaging, hairs on the scalp were removed by using an over-the-counter depilatory cream, and ultrasound gel was also applied on the scalp to ensure good ultrasound

coupling. During the imaging process, both the scalp and the skull were kept. Therefore, the imaging modality was completely non-invasive and non-destructive.

The SA-PA dual mode microscopy was used to noninvasively scan the mouse brain *in vivo*. Figure 8 presents the dual modal images of the mouse brain. The scanning range is 7.5 mm × 12 mm with a step size of 30 μm along x and y directions. Figure 8(a) is the photoacoustic MAP image. Color encodes the depth in the z direction. Since the high-sensitivity optical absorption at 532 nm in the hemoglobin domain, vessels generate strong PA signals under the illumination of the laser with a wavelength of 532 nm. Therefore, AR-PAM image clearly indicates the profile of the major vascular landmarks (sagittal sinus, coronal suture) under the scalp and the skull. However, it is hard to clearly image the structure of the cortex vessels by using a conventional optical camera [Fig. 8(c)], because of the strong optical scattering. In order to further verify the AR-PAM image in Fig. 8(a), we removed the scalp with the skull intact after imaging. The *in situ* anatomical photograph of the brain is shown in Fig. 8(d). The major vascular landmarks in AR-PAM image [Fig. 8(a)] agree well with the photograph in Fig. 8(d).

A SAM image was obtained by the microscope at the same time. In comparison to AR-PAM image, SAM image reveals different structural information. Since the serious acoustic impedance mismatch between the scalp, skull and the surrounding environment, strong US reflections occur at their interfaces. SAM implements US echoes to reconstruct the image, which indicates the distribution of the acoustic reflectors. Therefore, SAM image displays the skull clearly, as shown in Fig. 8(b). The SA-PA dual mode microscopy obtains the distribution of optical absorption (blood vessels), as well as the structure of acoustic scatterers (skull and scalp), simultaneously.

However, the negative effects of acoustic reflection could be easily noticed if we observe the imaging results from x–z and y–z cross-sections, as shown in Fig. 9. The four columns from left to right shown in Fig. 9 correspond to y–z cross-section B1, x–z cross-sections B2, B3, B4 pointed in Fig. 8, respectively. SAM images are displayed on the top row [Figs. 9(a), 9(d), 9(g), 9(j)]. Due to the acoustic impedance mismatch, the US echoes can reveal the profiles of the PDMS film layer (purple arrow), scalp (green arrow) and the skull (white arrow). Since the strongest reflection occurs on the interface between scalp and the skull, the MAP image of SAM [Fig. 8(b)] effectively manifests the structural information of the skull.

The middle row [Figs. 9(b), 9(e), 9(h), 9(k)] gives the original AR-PAM images before artifact suppression. The strongest PA signals are generated by vessels under the skull. PA waves of vessels propagate through skull, scalp, PDMS film layer, water in order, and finally reach the US transducer. Acoustic impedance mismatch between these layers induces multiple acoustic reflections, which form serious artifacts in the AR-PAM image. The red arrow, orange arrow, yellow arrow in Fig. 9(b) point out the reflected artifacts, which correspond to the artifacts indicated in Figs. 9(e) (red arrow), 9(h) (orange arrow), 9(k) (yellow arrow), respectively. Also, the blue arrow in Fig. 9(k) points out another position affected by artifacts. The real images are mixed with the artifacts and the PA imaging quality is badly degraded by acoustic reflections.

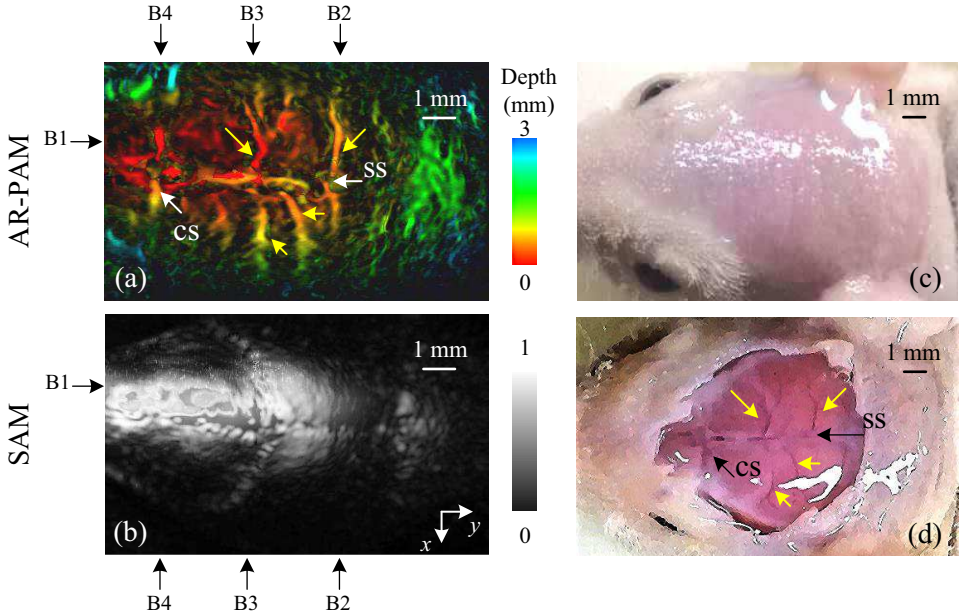

Fig. 8. Noninvasive *in-vivo* experiment of the mouse brain. (a) The MAP image of the mouse cortex vasculature obtained by AR-PAM. Color coding along the depth direction is applied on this image to represent the distribution of blood vessels on the depth direction. SS: sagittal sinus. CS: coronal suture. (b) The MAP image of the mouse skull and the scalp obtained by SAM. (c) Photograph taken after imaging, where the cortex vessels of the brain are invisible. (d) Photograph taken after imaging with the scalp removal, where the result in (a) agrees well with (d). The yellow arrows point out several major vascular landmarks and corresponding locations in (a) and (d). B1, B2, B3, B4 point out the positions of four sections in Fig. 9.

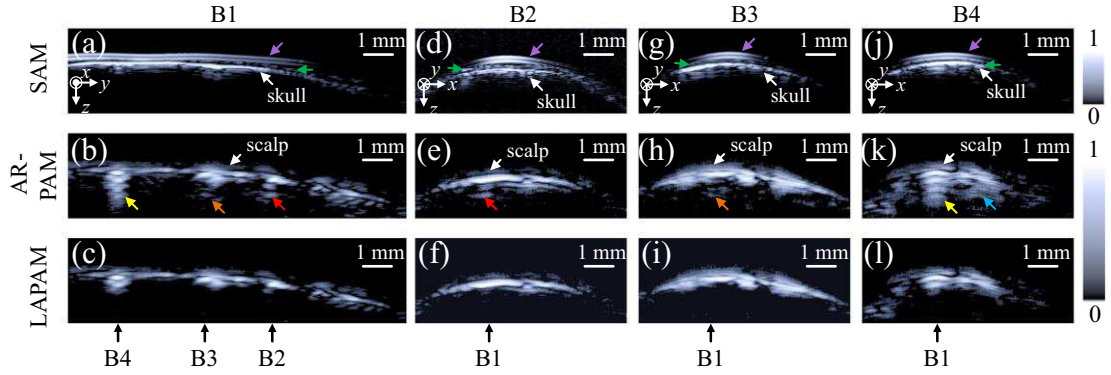

Fig. 9. Comparisons of the images in x–z and y–z sections obtained by SAM, conventional AR-PAM and the proposed method. The top row [(a), (d), (g), (j)] gives the SAM images of the y–z plane B1, x–z plane B2, B3, B4 marked in Fig. 8. The US echoes can reveal the profiles of the PDMS film layer (purple arrow), scalp (green arrow) and the skull (white arrow). The middle row [(b), (e), (h), (k)] shows the results obtained by a conventional AR-PAM scheme. The red arrow, orange arrow, yellow arrow in (b) point out the reflected artifacts, which correspond to the artifacts indicated in (e) (red arrow), (h) (orange arrow), (k) (yellow arrow), respectively. The corresponding LAPAM images are shown in the bottom row [(c), (f), (i), (l)], where the artifacts pointed out in the middle column are suppressed and the real images of vessels are still left.

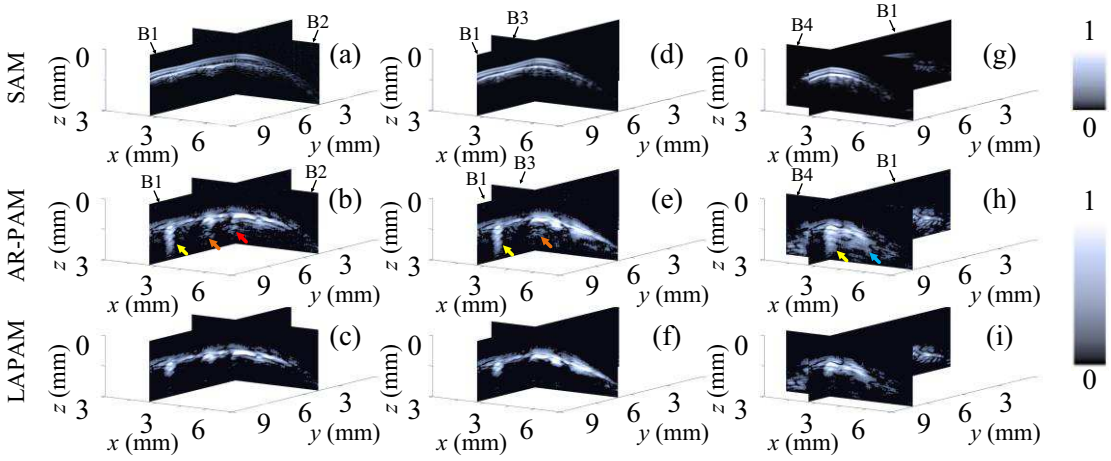

Fig. 10. Comparisons of the images in B1–B2 slices, B1–B3 slices, B1–B4 slices obtained by SAM, conventional AR-PAM and the proposed method. The top row [(a), (d) and (g)] gives the SAM images of the B1–B2 slices, B1–B3 slices, B1–B4 slices. The conventional AR-PAM results are shown on the middle row [(b), (e) and (h)] and the corresponding artifacts marked by red, orange, yellow, blue arrows in Fig. 9 are pointed out again. The corresponding artifact-suppressed LAPAM images are displayed on the bottom row [(c), (f) and (i)].

The bottom row [Figs. 9(c), 9(f), 9(i), 9(l)] shows the LAPAM images obtained by the proposed method. Since the acoustic impedance of the skull is about 4.69×10^6 kg/(m^2·s),[41] and the acoustic impedance of the tissue is about 1.65×10^6 kg/(m^2·s),[42] the correction factor $1/C$ used here is -3.35. The results demonstrate that the processing successfully suppresses the artifacts induced by the skull, scalp and the film, but keeps the real image of the vessels. This experiment verifies the practicality of the method in *in vivo* brain imaging.

For better comparison, Fig. 10 gives the profiles of B1–B2, B1–B3, B1–B4 slices on the left column, middle column, right column, respectively. The top row [Figs. 10(a), 10(d), 10(g)] gives the SAM images. The conventional AR-PAM results are shown on the middle row and the corresponding artifacts marked by red, orange, yellow, blue arrows in Fig. 9 are pointed out again. The artifact-suppressed LAPAM images are displayed on the bottom row, demonstrating the effectiveness of the proposed strategy.

6. Conclusion

In this work, we propose a LAPAM method to suppress the reflection artifacts caused by multilayered inhomogeneous media, therefore, improve the imaging quality of PAM in its application of imaging the brain of small animals through the scalp and the skull.

We find that when imaging optical absorbers below several acoustically inhomogeneous layers, the multiple reflections of PA signals will appear. Benefitting from the similarity of the propagation scheme between the PA signal and the US echo, the PA signal can be guided by the US echo to suppress the multi-reflections. Based on this finding, we combine conventional AR-PAM and SAM. Implementing our imaging system, the AR-PAM image and the SAM image can be obtained at one scan. And then we propose a method called LAPAM. In this method, we obtain a filter from the US echo to suppress

the multiple reflected artifacts and obtain the LAPAM image.

A phantom experiment of imaging several tungsten wires below several acoustic reflecting layers verifies the effectiveness of LAPAM. Finally, an *in-vivo* experiment of mouse brain imaging justifies the practicality of LAPAM for biomedical applications. Since multilayered inhomogeneous media often exist in biological tissues, such as the scalp and the skull above the brain tissue, there will be strong reflections that will degrade the quality of brain image. Therefore, the method of LAPAM improves the imaging quality of PAM in some biomedical applications by suppressing the reflection artifacts induced by multilayers, especially in brain imaging without destroying the scalp as well as skull *in vivo*.

Acknowledgements

Project supported by the National Natural Science Foundation of China (Grant Nos. 12027808, 11874217, 11834008, 81900875, and 81770973) and Natural Science Foundation of Jiangsu Province, China (Grant No. BK 20181077).

References

[1] Wang L V and Hu S 2012 *Science* **335** 1458
[2] Seong M and Chen S L 2020 *Sci. China Life Sci.* **63** 1798
[3] Ntziachristos V 2010 *Nat. Methods* **7** 603
[4] Zhang W, Li Y, Nguyen V P, Derouin K, Xia X, Paulus Y M and Wang X 2020 *J. Biomed. Opt.* **25** 066003
[5] Jin T, Guo H, Jiang H, Ke B and Xi L 2017 *Opt. Lett.* **42** 4434
[6] Yao J, Xia J and Wang L V 2016 *Ultrason Imaging* **38** 44
[7] Nguyen V P, Li Y, Qian W, Liu B, Tian C, Zhang W, Huang Z, Ponduri A, Tarnowski M, Wang X and Paulus Y M 2019 *Sci. Rep.* **9** 5945
[8] Tian C, Zhang W, Mordovanakis A, Wang X and Paulus Y M 2017 *Opt. Express* **25** 15947
[9] Moothanchery M, Seeni R Z, Xu C and Pramanik M 2017 *Biomed. Opt. Express* **8** 5483
[10] Tian C, Zhang W, Nguyen V P, Wang X and Paulus Y M 2018 *J. Vis. Exp.* **132** e57135
[11] Zhang H F, Maslov K, Stoica G and Wang L V 2006 *Nature Biotechnol.* **24** 848
[12] Leng X, Chapman W, Rao B, Nandy S, Chen R, Rais R, Gonzalez I, Zhou Q, Chatterjee D, Mutch M and Zhu Q 2018 *Biomed. Opt. Express* **9** 5159
[13] Yang X, Zhang Y, Zhao K, Zhao Y, Liu Y, Gong H, Luo Q and Zhu D 2016 *IEEE Trans. Med. Imaging* **35** 1903
[14] Yao J and Wang L V 2014 *Neurophoton* **1** 011003
[15] Stein E W, Maslov K and Wang L V 2009 *J. Appl. Phys.* **105** 102027
[16] Stein E W, Maslov K and Wang L V 2009 *J. Biomed. Opt.* **14** 020502
[17] Kneipp M, Turner J, Estrada H, Rebling J, Shoham S and Razansky D 2016 *J. Biophotonics* **9** 117
[18] Brunker J and Beard P 2016 *Sci. Rep.* **6** 20902
[19] Wang L, Xia J, Yao J, Maslov K and Wang L V 2013 *Phys. Rev. Lett.* **111** 204301
[20] Jeon S, Park J, Managuli R and Kim C 2019 *IEEE Trans. Med. Imaging* **38** 250
[21] Mohammadi L, Behnam H, Tavakkoli J and Avanaki K 2020 *Biomed. Opt. Express* **11** 5542
[22] Baik J W, Kim J Y, Cho S, Choi S, Kim J and Kim C 2020 *IEEE Trans. Med. Imaging* **39** 975
[23] Yang Y and Yang S H 2012 *Chin. Phys. B* **21** 054211
[24] Wang S, Tao C and Liu X 2013 *Chin. Phys. B* **22** 074303
[25] Chen W, Tao C, Nguyen N Q, Prager R W and Liu X 2020 *Opt. Lett.* **45** 3840
[26] Gao X, Tao C, Wang X and Liu X 2015 *Opt. Lett.* **40** 970
[27] Liu Z, Tao C and Liu X 2019 *Appl. Phys. Express* **12** 057001
[28] Dai N, Tao C, Gao X, Chen W, Zhang X and Liu X 2020 *Appl. Phys. Express* **13** 017005
[29] Lv X, Xu X, Feng Q, Zhang B, Ding Y and Liu Q 2020 *Chin. Phys. B* **29** 034301
[30] Mozaffarzadeh M, Varnosfaderani M H H, Sharma A, Pramanik M, Jong N and Verweij M D 2019 *J. Biophotonics* **12** e201900133
[31] Guo Z, Li Y and Chen S L 2018 *Opt. Lett.* **43** 1119
[32] Moothanchery M and Pramanik M 2017 *Sensors* **17** 357
[33] Singh M K A, Jaeger M, Frenz M and Steenbergen W 2016 *Biomed. Opt. Express* **7** 2955
[34] Singh M K A and Steenbergen W 2015 *Photoacoustics* **3** 123
[35] Allman D, Reiter A and Bell M A L 2018 *IEEE Trans. Med. Imaging* **37** 1464
[36] Nguyen H N Y, Hussain A and Steenbergen W 2018 *Biomed. Opt. Express* **9** 4613
[37] Chen W, Tao C and Liu X 2019 *Opt. Lett.* **44** 1273
[38] Zhang X, Qian X, Tao C and Liu X 2018 *Ultrasound Med. Biol.* **44** 1110
[39] Maev R G 2013 *Advances in Acoustic Microscopy and High Resolution Imaging from Principles to Applications* (Weinheim: Wiley-VCH Verlag & Co. KGaA) p. 98
[40] Rahman M F A, Arshad M R, Manaf A A and Yaacob M I H 2012 *Indian J. Mar. Sci.* **41** 557
[41] Liang B, Liu W, Zhan Q, Li M, Zhuang M, Liu Q H and Yao J 2019 *J. Biophotonics* **12** e201800466
[42] Kobayashi K, Yoshida S, Saijo Y and Hozumi N 2014 *Ultrasonics* **54** 1922